10.2514/6.2017-3658

18th AIAA/ISSMO Multidisciplinary Analysis and Optimization Conference, 5 – 9 June 2017, Denver, Colorado

# Reduction of Airframe Noise Components Using a Discrete Adjoint Approach

Beckett Y. Zhou,* Tim Albring,† and Nicolas R. Gauger‡
*Chair for Scientific Computing, TU Kaiserslautern*
*Bldg 34, Paul-Ehrlich-Strasse, 67663 Kaiserslautern, Germany*

Carlos R. Ilario da Silva,§ Thomas D. Economon,¶ and Juan J. Alonso ‖
*Department of Aeronautics and Astronautics, Stanford University*
*Stanford, CA 94305, U.S.A.*



**In this paper, we present an unsteady aerodynamic and aeroacoustic optimization framework in which algorithmic differentiation (AD) is applied to the open-source multi-physics solver SU2 to obtain design sensitivities. An AD-based consistent discrete adjoint solver is developed which directly inherits the convergence properties of the primal flow solver due to the differentiation of the entire nonlinear fixed-point iterator. In addition, a coupled 3-dimensional CFD-CAA far-field noise prediction framework using a permeable surface Ffowcs Williams-Hawkings approach in time domain is also developed. The resultant AD-based discrete adjoint solver is applied to the reduction of airframe component noise. The results suggest that the unsteady adjoint information provided by this AD-based discrete adjoint framework is accurate and robust, due to the algorithmic differentiation of the entire design chain including the dynamic mesh movement routine and various turbulence model, as well as the hybrid CFD-CAA model. This study also compares the optimization results obtained on the basis of 3D unsteady Reynolds-averaged NavierStokes equations (URANS simualtions) and analyze them using scale-resolving simulations of higher fidelity.**

## I. Introduction

Ambitious noise reduction goals have been set by aviation regulatory bodies all around the world in order to curb the rising noise pollution as a result of the rapid growth of air travel. Aircraft noise can be broadly divided into two categories: engine noise and airframe noise. In the past 40 years, engine noise has been significantly reduced due to the transition towards high-bypass ratio turbofan engines. Under approach conditions for most modern aircraft, the airframe noise contribution is now on-par with that of the engine noise, even surpassing it for some aircraft.

Airframe noise consists of components from the landing gear and high-lift systems, as well as various cavities such as the landing gear well. With noise sources from these components interacting in a complex manner and combining on a logarithmic scale, airframe noise reduction proves to be challenging – all sources must be reduced by commensurate amount to effect significant perceived noise reduction.[1]

It is therefore essential for the aviation community to have accurate simulation tools to visualize and understand noise sources associated with various airframe components and their effect on the far-field noise signature of the aircraft. Furthermore, efficient and robust design optimization tools must be developed in parallel to modify the existing designs in a noise-reducing direction without sacrificing aerodynamic performances. The latter requirement is even stronger in the case of development of unconventional aircraft configurations for which much of the design space remains uncharted.

*Ph.D. Candidate, Student Member AIAA, yuxiang.zhou@scicomp.uni-kl.de
†Ph.D. Candidate, tim.albring@scicomp.uni-kl.de
‡Professor, Senior Member AIAA, nicolas.gauger@scicomp.uni-kl.de
§Visiting Senior Research Associate, Associate Member AIAA, carlos.ilario@stanford.edu
¶Postdoctoral Scholar, Student Member AIAA, economon@stanford.edu
‖Professor, Associate Fellow AIAA, jjalonso@stanford.edu

To help tackle the unavoidably large number of control variables involved in such design efforts, adjoint-based methods is a good method of choice due to the fact that the computational cost of evaluating the design sensitivities is independent of the number of design variables. Since the advent of adjoint-based methods,[2,3] much work has been done on aerodynamic shape optimization in both steady and unsteady settings.[4–10]

Under the discrete framework, the effort of the adjoint implementation can be eased by the use of algorithmic differentiation (AD), replacing the laborious and error-prone hand-differentiation of the discretized equations. This however, is not the only advantage of AD-based adjoint. By construction, AD-based adjoints are accurate to machine precision as they do not incur any roundoff or truncation error. In addition, the *frozen turbulence* assumption typically used in many URANS-based adjoint formulations is eliminated, since the turbulence models while not analytically differentiable are still *algorithmically* differentiable. The application of AD also leads to robust and consistent adjoints in that the adjoint solver inherit the same convergence properties as the primal solver. Lastly, if the operator overloading AD method is used with expression template technique in C++,[11] the resultant discrete adjoint framework offers extra flexibility – the adjoint solver can be automatically updated with primal code modification and one can easily define any objective function from any state variable. This is an extremely attractive characteristic for unsteady optimization problems in the multidisciplinary setting using a suite of multi-physics solvers where the objective function may be different depending on the type of problems being addressed. AD-based discrete adjoint has been applied to steady aerodynamic shape design problems by Bischof et al.[12] and Gauger et al.[13] More recently, it was successfully applied by Nemeli et al.[14] in the unsteady setting to the active flow control of an industry-relevant high-lift configuration HIREX from Airbus.

Nowadays, most of the aeroacosutic community focuses on noise predictions on the basis of scale-resolving simulations such as large-eddy simulation (LES) or variants of the detached-eddy simulation (DES). These simulations remain computationally daunting for optimization. A natural question that arises is then whether optimization performed based on simulations of lower fidelty such as URANS can provide reliable design updates – is a noise-minimized design determined by a URANS-based optimization still considered optimal when analyzed with high-fidelty turbulence resolvign simulations or even experimental measurements? In this work, to shed some light on this question, we perform noise optimization using a 3D URANS-FWH framework and compare the designs using a delayed detached-eddy simulation (DDES).

In this paper, we present the extension of our previous work[22] on the development of an AD-based discrete adjoint framework on an open source multi-physics suite SU2[15] for applications to unsteady aerodynamic and aeroacoustic optimization problems. The remainder of the paper is organized as follows. In Section II, the unsteady SU2 solver including a coupled CFD-CAA model using a permeable surface Ffowcs Williams-Hawkings (FW-H) approach as well as the optimization framework based on discrete adjoint and AD are presented. Section III presents verification results for the hybrid CFD-FWH far-field noise prediction framework as well as the validation of coupled CFD-CAA adjoint. Optimization results are presented in Section IV while the conclusion and outlook for future work are outlined in Section V.

## II. Unsteady Aerodynamic and Aeroacoustic Optimization Framework

### II.A. Unsteady Multi-Physics Solver SU2

The Stanford University Unstructured (SU2) open source software suite was specifically developed for solving problems governed by partial differential equations (PDEs) and PDE-constraned optimization problems. It was developed with the aerodynamic shape optimization problems in mind. Therefore the suite is centered around a RANS solver capable of simulating compressible, turbulent flows commonly found in problems in aerospace engineering. The governing equations are spatially discretized using the finite volume method, on unstructured meshes. A number of convective fluxes discretization schemes have been implemented, such as the Jameson-Schimdt-Turkel (JST) scheme and the upwind Roe scheme. The turbulence can be either modeled by the Spalart-Allmaras(S-A) model or the Menter Shear Stress Transport (SST) Model. For unsteady flows, a dual time-stepping method can be used to obtain time-accurate solutions. SU2 suite has recently seen extensions in the multi-disciplinary setting such as the inclusion of a wave equation solver and a structural solver, making it well-suited for the unsteady multi-physics problems considered in this work. The DDES-SA simulation used in this work is implemented in a parallel effort by Molina et al.[24]

For the sake of conciseness, details regarding the formulations and implementations of the SU2 solver suite will not be presented in this paper. Further details such as mesh deformation, dynamic mesh movement, multigrid implementations, validation and verification cases, as well as the continuous adjoint framework developed in tandem with SU2, the readers are referred to the published work by Palacios et al.[10,15] of the SU2 team. In the next section we

direct the attention of the readers to a new coupled CFD-CAA far-field noise prediction framework developed for the current work.

### II.B. Coupled CFD-CAA Noise Prediction using a Permeable Surface Ffowcs Williams-Hawkings Approach

It is known for turbulent flows at low Mach numbers, direct computations of far-field noise is computationally prohibitive.[16] A common way to perform far-field noise prediction is then to adopt a hybrid CFD-CAA approach in which the near-field noise source region is computed using a high-fidelity CFD model and then propagated to the far-field using a computationally cheaper wave equation like CAA model. To that end, integral methods based on the Kirchhoff or Ffowcs Williams-Hawkings (FW-H) formulations offer a more efficient approach for calculating acoustic pressure at arbitrary observer locations by performing boundary integrals once the appropriate field data is known. In this manner, the radiated noise from a complex system can be calculated given the near-field flow data supplied by a CFD solution. In this work, we develop a coupled CFD-CAA far-field noise prediction framework using a permeable surface Ffowcs Williams-Hawkings approach.

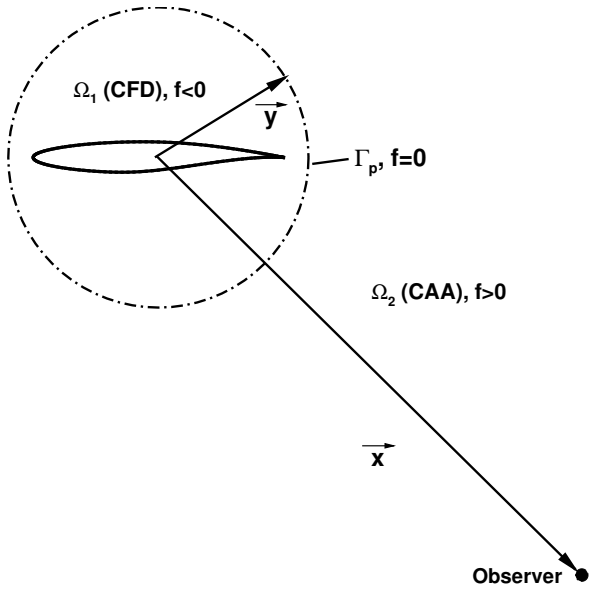


**Figure 1. Permeable control surface $\Gamma_p$ separating the CFD and CAA domains**

The permeable FW-H formulation distinguishes itself from its original formulation in that it allows fluid to flow through the discontinuity surface. Consequently, one can define any arbitrary smooth surrounding surface $\Gamma_p$ around the aerodynamic body $S$ where details of the flow field are extracted and the noise source can be propagated to the far-field. A schematic of such permeable surface is shown on Figure 1. The fluid domain is therefore divided into two regions – the near-field CFD region $\Omega_1$ and far-field CAA region $\Omega_2$. Further, we define the shape of $\Gamma_p$ by a function, $f = 0$, such that $f < 0$ inside the control surface and $f > 0$ outside the control surface.

A key difference between this work and an earlier work by Economon et al.[9] is that in that work the permeable FW-H formulation in the wave equation form is solved directly in time using a finite element method (FEM). In this work we follow the boundary integral formulation presented by Di Francescantonio,[18] which rewrites the original FW-H into the permeable surface form as follows:

$$\Box^2[c^2(\rho-\rho_o)] = \frac{\partial}{\partial t}[\rho_o U_n \delta(f)] - \frac{\partial}{\partial x_i}[L'_{ij} n_j \delta(f)] + \frac{\partial^2 T_{ij}}{\partial x_i \partial x_j}. \tag{1}$$

where

$$U_i = u_i + [(\rho/\rho_o) - 1](u_i - v_i) \tag{2}$$

$$L_{ij} = P_{ij} - p_o\delta_{ij} + \rho u_i(u_j - v_j), \tag{3}$$

$$T_{ij} = P'_{ij} + \rho u_i u_j - c^2(\rho - \rho_o)\delta_{ij}. \tag{4}$$

Note that $\rho$ is the density, $u_{i,j,k}$ is the flow velocity, $v_{i,j,k}$ is the velocity of the control surface $\Gamma_p$. The subscript $o$ denotes ambient conditions while the superscript $'$ denotes perturbation values. $P_{ij}$ is the compressive stress tensor.

By convoluting with a free space Green's function, a boundary integral form can be obtained. Following the derivation of Farassat's formulation 1A,[19] time derivatives with respect to observer time can be moved inside of the integrals and adjusted to be with respect to source time. This manipulation can offer some benefits during numerical implementation. Lastly, by assuming a non-deforming surface which is far enough away from the source to contain all non-linearities, the quadrupole volume terms can be removed, and the following boundary integral expression is

recovered for the pressure at an arbitrary observer location,

$$4\pi p'_{obs} = \int_{\Gamma_p} \left[ \frac{\rho_o(\dot{U}_i n_i + U_i \dot{n}_i)}{r|1-M_r|^2} \right]_{ret} d\Gamma_p + \int_{\Gamma_p} \left[ \frac{\rho_o U_i n_i K}{r^2|1-M_r|^3} \right]_{ret} d\Gamma_p + \frac{1}{c} \int_{\Gamma_p} \left[ \frac{\dot{F}_i \hat{r}_i}{r|1-M_r|^2} \right]_{ret} d\Gamma_p + \int_{\Gamma_p} \left[ \frac{F_i \hat{r}_i - F_i M_i}{r^2|1-M_r|^2} \right]_{ret} d\Gamma_p + \frac{1}{c} \int_{\Gamma_p} \left[ \frac{F_i \hat{r}_i K}{r^2|1-M_r|^3} \right]_{ret} d\Gamma_p. \quad (5)$$

where $K = \dot{M}_i \hat{r}_i r + M_r c - M^2 c$ and $F_i = L_{ij} n_j$. For a stationary permeable surface, all terms involving $M$ or $M_r$ become zero and Equation 5 simplifies to:

$$4\pi p'_{obs} = \int_{\Gamma_p} \left[ \frac{\rho_o \dot{U}_n}{r} \right]_{ret} d\Gamma_p + \frac{1}{c} \int_{\Gamma_p} \left[ \frac{\dot{F}_r}{r} \right]_{ret} d\Gamma_p + \int_{\Gamma_p} \left[ \frac{F_r}{r^2} \right]_{ret} d\Gamma_p. \quad (6)$$

The equation above is applicable in two or three dimensions depending on the free-space Green function used. For the types of low speed flows examined in this work, the contribution of quadrupole source is typically negligible (as it scales with $M^4$) in comparison to the monopole and dipole terms. In addition, the inclusion of the quadrupole term would entail the computationally expensive evaluation of a surface integral over the entire domain outside of the permeable surface. Therefore, the quadrupole term is neglected in the evaluation of Equation 5 for problems presented in this abstract. For jet and shear-dominated flows $\tilde{T}_{ij}$ is not negligible. The CAA module is implemented and interfaced with the remainder of the SU2 suite as follows: an unsteady flow simulation is first performed. At every time step, the primitive flow variables at each point on the permeable surface are extracted and the monopole and dipole source terms computed using Equations 2 and 3. At the end of the CFD simulation, the respective mean values are subtracted from $U_i$ and $L_{ij}$ as they correspond to zero frequency components which do not generate any noise. The pressure fluctuation in time domain can be computed by numerically integrating along the permeable surface, for each observer location $\vec{\mathbf{x}}$. Note that the integrands are written in 'retarded time' and must be interpolated from the source time ($\tau$) at each panel on the FWH surface to observer time ($t = \tau + r/c$) before the surface integral can be taken.

### II.C. AD-based Unsteady Discrete Adjoint Framework

The implementation of the discrete adjoint formulation in this work is eased by the use of automatic differentiation (AD) [a], eliminating the error-prone hand-differentiation of the discretized equations. AD was developed based on the observation that any simulation code, regardless of its complexity is merely a sequence of elementary operations whose differentiation rules are well known. Therefore, by successive applications of the chain-rule through the computer program, it is possible to compute both the simulation output and its derivative with respect to prescribed design variables simultaneously. A remarkable feature of AD, owing to its construction, is that it does not incur any truncation errors compared to the traditional finite difference method. In particular, the derivatives are accurate to machine accuracy. This is a very attractive characteristic of AD, since accurate evaluation of the gradient requires exact differentiation of the fixed point iterator $G^n$ as evidenced by Equations 20 and 21 in the following discussion.

The AD can be performed in the forward and reverse (adjoint) mode. The forward mode, albeit exact, requires one evaluation for each component of the gradient vector. In contrast, the reverse mode is capable of computing the entire gradient vector in one stroke of the forward and reverse simulation in time. For this reason, the reverse mode is also referred to as the adjoint mode. The one-stroke gradient computation of the reverse mode AD is achieved at the expense of high memory requirement due to the need to save all intermediate variables in an unsteady computation. For this reason, wherever the adjoint mode is used in this study, it is always implemented in conjunction with the memory-saving checkpointing technique, which stores the flow solution at certain points in time during the forward sweep as *checkpoints*. The flow solutions are then recomputed from these checkpoints in the reverse sweep for adjoint variables. The maximum number of time steps allowable between the two consecutive checkpoints is dictated by the memory available at each core. For long time computations, the many checkpoints required results in high hard disk storage requirement and an increase in run time due to the need to recompute the flow solutions as well as reading and writing of large volumes of data at each checkpoint. A good discussion of the two AD modes along with checkpointing techniques can be found in.[20,21]

Now we present our AD-based unsteady discrete adjoint framework using a simple system of PDEs as an example. For the sake of brevity, influences of the mesh are omitted. Consider a system of semi-discretized PDEs as follows:

$$\frac{dU}{dt} + R(U) = 0 \quad (7)$$

[a] performed using AD tool ADEPT[11]

where $U$ is the spatially discretized state vector and $R(U)$ is the discrete spatial residual vector. For the sake of illustration, we assume the second-order backward difference is used for time discretization, which leads to the following system of equations:

$$R^*(U^n) = \frac{3}{2\Delta t}U^n + R(U^n) - \frac{2}{\Delta t}U^{n-1} + \frac{1}{2\Delta t}U^{n-2} = 0, \qquad n = 1,\ldots,N \tag{8}$$

The application of dual-time stepping method then solves the following problem through a fictitious time $\tau$ to converge to a steady state solution in (8):

$$\frac{dU^n}{d\tau} + R^*(U^n) = 0 \tag{9}$$

Further assume the implicit Euler method is used to time march the above equation to steady state.

$$U^n_{p+1} - U^n_p + \Delta\tau R^*(U^n_{p+1}) = 0, \qquad p = 1,\ldots,M \tag{10}$$

The resultant nonlinear system can be linearized around $U^n_p$ to solve for the state $U^n_{p+1}$

$$U^n_{p+1} - U^n_p + \Delta\tau\left[R^*(U^n_p) + \frac{\partial R^*}{\partial U}\bigg|^n_p (U^n_{p+1} - U^n_p)\right] = 0, \qquad p = 1,\ldots,M \tag{11}$$

This can be written in the form of a fixed-point iteration:

$$U^n_{p+1} = G^n(U^n_p, U^{n-1}, U^{n-2}), \qquad p = 1,\ldots,M, \quad n = 1,\ldots,N \tag{12}$$

where $G^n$ represents an iteration of the pseudo time stepping. $U^{n-1}$ and $U^{n-2}$ are the converged state vectors at time iterations $n-1$ and $n-2$ respectively. The fixed point iteration converges to the numerical solution $U^n$:

$$U^n = G^n(U^n, U^{n-1}, U^{n-2}), \qquad n = 1,\ldots,N \tag{13}$$

The discrete optimization problem can then be posed as:

$$\min_{\alpha} \quad J = f(U^{N_*},\ldots,U^N,\alpha) \tag{14}$$

$$\text{subject to} \quad U^n = G^n(U^n, U^{n-1}, U^{n-2}, \alpha), \qquad n = 1,\ldots,N \tag{15}$$

where $\alpha$ is the vector of design variables and the objective function $J$ is evaluated between $N_* \leq n \leq N$. One can express the Lagrangian associated with the above constrained optimization problem as follows:

$$L = f(U^{N_*},\ldots,U^N,\alpha) - \sum_{n=1}^{N}[(\bar{U}^n)^T(U^n - G^n(U^n, U^{n-1}, U^{n-2}, \alpha))] \tag{16}$$

where $\bar{U}^n$ is the adjoint state vector at time level $n$. The first order optimality conditions are given by:

$$\frac{\partial L}{\partial \bar{U}^n} = 0, \quad n = 1,\ldots,N \qquad \text{(State equations)} \tag{17}$$

$$\frac{\partial L}{\partial U^n} = 0, \quad n = 1,\ldots,N \qquad \text{(Adjoint equations)} \tag{18}$$

$$\frac{\partial L}{\partial \alpha} = 0, \qquad \text{(Control equation)} \tag{19}$$

From (18), the unsteady discrete adjoint equations can be derived in the fixed point form as:

$$\bar{U}^n_{i+1} = \left(\frac{\partial G^n}{\partial U^n}\right)^T \bar{U}^n_i + \left(\frac{\partial G^{n+1}}{\partial U^n}\right)^T \bar{U}^{n+1} + \left(\frac{\partial G^{n+2}}{\partial U^n}\right)^T \bar{U}^{n+2} + \left(\frac{\partial f}{\partial U^n}\right)^T, \; n = N,\ldots,1 \tag{20}$$

where $\bar{U}^{n+1}$ and $\bar{U}^{n+2}$ are converged adjoint state vectors at time levels $n+1$ and $n+2$. The unsteady adjoint equations above are solved backward in time. At each time level $n$ we iterate through inner iteration $i$ until we have converged to $\bar{U}^n$. The highlighted terms here are evaluated in reverse mode AD at each iteration. To do so, reverse accumulation[20]

is performed at the beginning of each time level $n$ to store the computational graph by evaluating $G$ using converged state solution $U_n$. Then each inner iteration $i$ proceeds by re-evaulating the tape using the updated adjoint vector $\bar{U}_i^n$, giving the highlighted terms. This continues within each time level $n$ until the adjoint vector has converged to $\bar{U}^n$. Note that $\frac{\partial f}{\partial U^n} = 0$ for $n < N_*$. The sensitivity gradient can then be computed from the adjoint solutions:

$$\frac{dL}{d\alpha} = \frac{\partial f}{\partial \alpha} + \sum_{n=1}^{N} \left( (\bar{U}^n)^T \frac{\partial G^n}{\partial \alpha} \right) \tag{21}$$

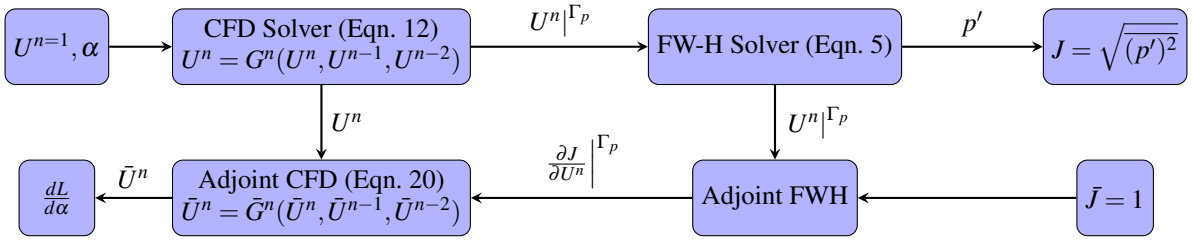


**Figure 2. Computational chain of the coupled CFD-FWH noise prediction and optimization framework**

The computational chain for the coupled CFD-FWH noise prediction and noise-adjoint framework is outlined on Figure 2. In the primal phase, unsteady flow field $U^n$ is realized at each time step $n$ by the SU2 CFD solver via Equation 12. $U^n|^{\Gamma_p}$ denotes the conservative flow variables at time step $n$ extracted from the FW-H surface $\Gamma_p$ which are then passed to the FW-H solver for far-field noise computation via Equation 5. In the adjoint phase, $\frac{\partial J}{\partial U^n}\Big|^{\Gamma_p}$ denotes the sensitivity of the noise objective with respect to conservative flow variables evaluated $\Gamma_p$ by the adjoint FW-H solver using $U^n|^{\Gamma_p}$, which is accumulated to the fixed-point iteration for the adjoint flow variables $\bar{U}^n$ in the adjoint CFD solver (Equation 20).

In this work, we apply the operator overloading AD method with expression template technique[11] to the *SU*2 suite. This leads to additional flexibilities in the resultant discrete adjoint framework – the adjoint solver can be automatically updated with primal code modification and one can easily define any objective function from any state variable. This is an extremely attractive characteristic for unsteady optimization problems in the multidisciplinary setting using a suite of multi-physics solvers where the objective function may be different depending on the type of problems being addressed.

## III. Verification and Validation

### III.A. Verification of the Hybrid CFD-FWH Solver

To validate the hybrid CFD-FWH noise prediction framework, we place monopole source radiating sound at a specified frequency at the origin of a 3-D spatial domain. A point source has a well-known analytic form for the resulting spherically-symmetric perturbation pressure field.[27] An porous spherical FWH surface of radius $r_{FWH} = 0.1m$ surrounds the point source. The primitive flow variables on the FWH surface are computed analytically and used to evaluate the noise sources in Equations 2 and 3. The pressure fluctuations at three radial positions ($r = 1.0m$, $2.0m$ and $4.0m$) are evaluated using the 3D FWH solver (Equation 5) and compared with analytical pressure fluctuations at these positions. As shown on Figure 3, the agreement between the analytic solution and 3D time-domain FWH results is excellent at all three microphone positions. The accuracy of the 3D frequency-domain implementation is also quite good except at the ends of the data where windowing needs to be used. Also, note that the $1/r$ delay law for the pressure fluctuation amplitude is almost perfectly observed as the microphone is progressively moved further from the source.

### III.B. Validation of Coupled CFD-CAA Adjoint

The SU2 suite has been differentiated using AD in both forward and reverse (adjoint) modes. Furthermore, checkpointing and reverse accumulation have also been implemented for the adjoint mode at each time iteration. For noise-minimization cases, the objective function is defined as the root-mean-square of the acoustic pressure averaged over $N_{obs}$ observer locations. The noise-specific coupled sensitivities are computed as outlined in Section II.C.

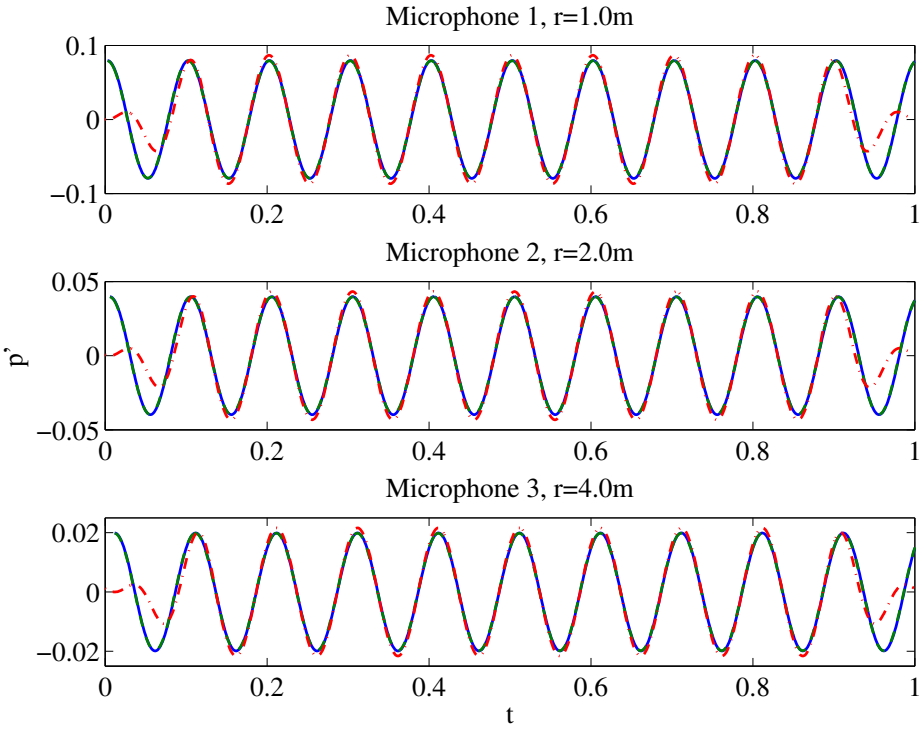


**Figure 3. Comparison of acoustic signals at three far-field microphone positions in the monopole source case (——: Analytic Signal; - - - : Time Domain FWH; -·-·-: Frequency Domain FWH)**

The coupled aeroacoustic sensitivities are validated for both laminar and turbulent flows via a cylinder vortex shedding test case. The surface sensitivities at 18 different circumferential positions on the cylinder surface are computed using both second order central difference and AD-based adjoint over 10 time steps. The comparisons are shown on Figure 4 (a) for the laminar case and Figure 4 (b) for the turbulent case. It is clear that AD-based adjoint attains very good accuracy. It must also be noted that as the integration time increases, the accuracy of finite difference will deteriorate, often to the order of the sensitivity itself, while AD-based adjoint incurs no round-off error and maintains high accuracy over long integration times.

# IV. Optimization Results

## IV.A. Minimization of Rod-Airfoil Interaction Noise

In this test case, we apply the AD-based discrete adjoint framework to optimize the shape of a NACA0012 airfoil section subjected to the turbulent wake of an upstream cylinder, so as to reduce far-field noise at three radiation angles.

The NACA0012 airfoil section with a chord length of $C = 0.1m$ and a span of $S = 0.5C$ is positioned at a distance of $0.7C$ downstream of a cylinder with diameter $D = 0.1C$. The inflow velocity is $72m/s$ with a Reynolds number based on the airfoil chord of $Re_C = 4.8 \times 10^5$. Under these conditions, the laminar boundary layer separation from the upstream cylinder quickly turns turbulent in the wake before impinging upon the leading edge of the airfoil. The farfield noise spectra exhibit both a clear tonal component corresponding to the periodic vortex shedding of the cylinder and a broadband component due to the turbulent wake impingement on the airfoil leading edge.

The computational mesh consists of 2.8 million cells with with 220 points around the rod, 310 points around the airfoil in the circumferential direction and 30 points in the spanwise direction, as shown on Figure 5(a). The nondimensional wall distance $y^+ \sim 1$ for both the rod and the cylinder. Relative dimensions of the computational domain as well as the location of the porous FWH surface are shown on Figure 5(b).

For a noise-minimization problem, the objective function is defined as the time-averaged pressure fluctuation

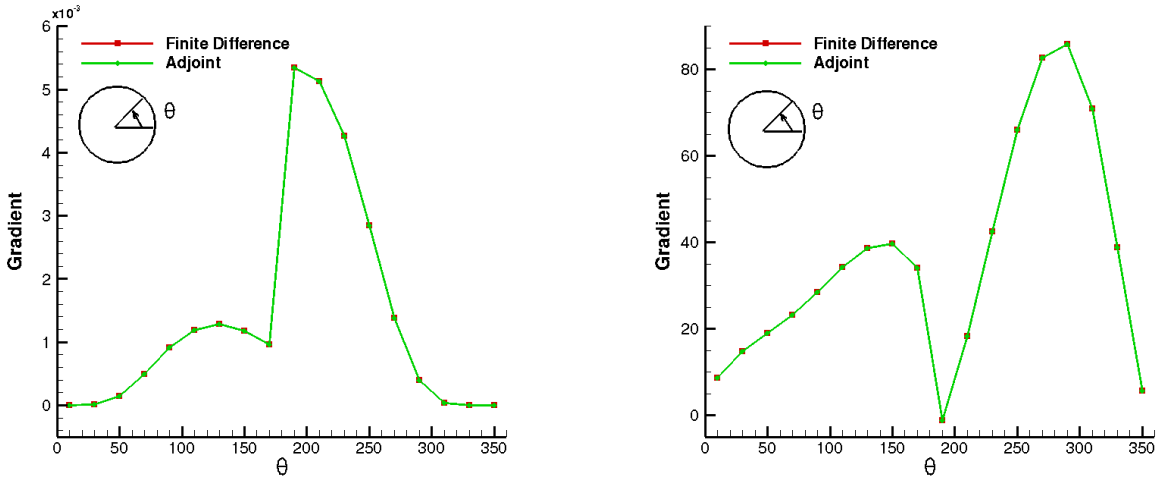


(a) Laminar (b) Turbulent

**Figure 4. Comparison between the gradients computed using finite difference (second order central difference with a step size of $10^{-6}$) and adjoint mode of AD, at various angular positions around the cylinder surface.**

within the periodic steady state at an observer location:

$$J_N = \frac{1}{N_{obs}} \sum_{m=1}^{N_{obs}} \sqrt{\frac{1}{N-N_*} \sum_{n=N_*+1}^{N} (p'_{n,m})^2} \tag{22}$$

where $p'_{n,m}$ is the pressure fluctuation at time level $n$ and observer location $m$ computed using the frequency domain FW-H solver introduced in Section II.B . Three far-field microphones are placed at a constant distance of $r = 100C$ from the wing leading edge, at three angular positions (45°, 90° and 135°). $N$ is the total number of time steps and $N_*$ is the number of time steps before entering the optimization window in which the magnitude of the pressure fluctuation is to be minimized. In this case $N_* = 700$ and the optimization window contains 5 periods of cylinder shedding. For the optimization, we constrain the shape deformation to a 2D section extruded in the spanwise direction, even though the adjoint solution is based on full 3D URANS-FWH computations.

The optimization is performed for 9 design updates and achieves a 33% reduction in the objective function, as shown on Figure 6(a). Figure 6(b) shows the evolution of the upper surface of the airfoil in the first 6 design updates. Note that the optimizer does not try to reduce the thickness of the airfoil section even though no thickness constraints are imposed. Instead, it progressively introduces more waviness in the upper and lower surfaces at each design update, especially in the leading edge region. This is not surprising as a round leading edge is known to result in less impingement noise of the turbulent wake than a sharp one. It is also interesting to note that a number of other works, also remarked on the efficacy of surface waviness in both spanwise and streamwise directions for drag and noise reduction purposes.

The pressure fluctuations of the baseline and optimized configurations at three aforementioned farfield microphone positions are plotted on Figure 7. Clearly, surface waviness indeed leads to significant reduction on the overall sound pressure level (OASPL) – up to 3dB reduction is obtained.

What is also worth noting is that the optimizer only introduces waviness in the streamwise but not in the spanwise direction. This is evident in the surface noise sensitivity plots on Figure 8 which show the both the streamwise and normal noise sensitivities to be uniform in the spanwise direction. This is due to the fact that the turbulent wake breakdown in the cylinder-airfoil gap cannot be resolved using the URANS-SA simulation. Consequently, spanwisely coherent vortices impinge upon the airfoil leading edge, as shown on Figure 9(a) – a URANS-SA computation performed on a denser, 4 million-element mesh. Presumably, an optimization performed on the basis of a turbulence-resolving simualtions such as LES or DES can reveal opportunities in introducing spanwise variations in the leading or trailing edge. Figure 9(b) shows a DDES-SA simluation computed using the same mesh which clearly captures finer turbulent structures than URANS-SA.

In this work, we analyze the baseline and optimized designs using DDES-SA-FWH simulations. That is, the hydrodynamic field is computed using DDES-SA and the noise source is propagated to the farfield microphone positions

using the 3D time-domain FWH method. Optimizations based on scale-resolving simulations are deferred for future studies. Figure 10 compares the snapshots of the nearfield spanwise vorticity on the mid-span plane, evaluated after 60 flow passage time units. Surface waviness in the optimized design appears to keep the noise-generating vortical structures closer to the airfoil body. Based on the DDES-SA simulations, farfield acoustics are computed using FWH. To that end, acoustic samples are collected after 50 flow passage time units to allow the transient effects to pass. The farfield acoustics are then computed based on 15000 samples which correspond to approximately 40 cycles of lift fluctuation on the airfoil. Figure 11(a) compares the pressure fluctuations of the baseline and optimized configurations at three farfield microphone positions. The objective function is reduced by $\sim 45\%$ as opposed to 33% predicted by URANS-SA. The OASPL is reduced by up to 6dB in the normal direction, as shown on Figure 11(b). Comparison of the noise spectra at the three microphone positions reveals that the peak SPL is reduced by 5-6dB in the optimized configuration. The peak frequency of $St = 0.19$ in the baseline configuration as reported by experimental data is also well-captured by the DDES-SA solver. Note that although the peak SPL at the three microphone positions have not been shifted towards higher frequency in the optimized design, noise reduction in the broadband range is not omni-directional. This is not surprising since the objective function is defined as the root-mean-square of the acoustic pressure which corresponds to the OASPL. To explicitly target the broadband noise, optimizations must be performed on the basis of turbulence-resolving simulations with the objective function redefined to penalize high frequency noise components (2-10 KHz) directly.



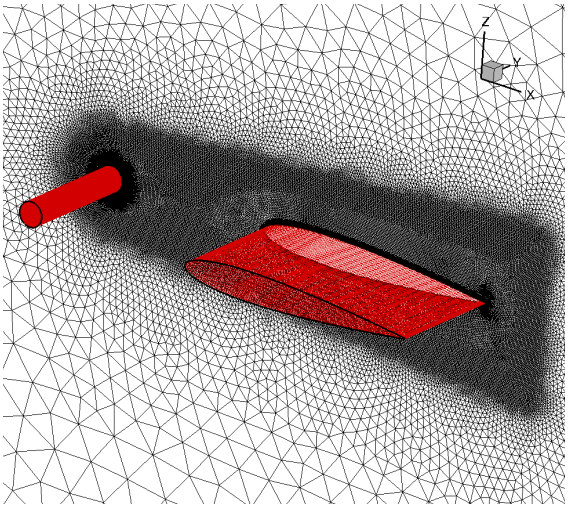


(a) Computational Mesh

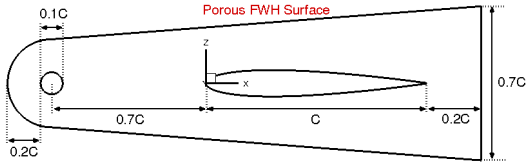


(b) Computational domain showing location of the porous FWH surface

**Figure 5. Computational mesh and sketch of computational domain showing relative dimensions of the rod and airfoil configuration as well as the location of the porous FWH surface**

## V. Conclusion and Outlook

In this paper, we present an unsteady aerodynamic and aeroacoustic optimization framework in which algorithmic differentiation (AD) is applied to the open-source multi-physics solver SU2 to obtain design sensitivities. An AD-based consistent discrete adjoint solver is developed which directly inherits the convergence properties of the primal flow solver due to the differentiation of the entire nonlinear fixed-point iterator. This includes the differentiation of the dynamic mesh movement routine and various turbulence model, as well as the hybrid CFD-CAA design chain – all of which can be cumbersome and error-prone using the continuous adjoint and hand-discrete approaches.

The results demonstrate that the unsteady adjoint information provided by this AD-based discrete adjoint framework is accurate and robust. Farfield noise minimization of a rod-airfoil configuration based on 3D URANS-FWH simulations is performed. The baseline and optimized designs are analyzed using turbulence-resolving DDES-SA simulations. The results indicate that although the optimal configuration determined by the URANS-based optimization also performs well when analyzed with DDES-SA and even exceeds the prediction of the original URANS simulation, to allow higher degrees of freedom, namely to introduce spanwise variations, scale-resolving simulations must be used in the optimization loop. Furthermore, to scale-resolving simulations are also necessary to directly tackle the

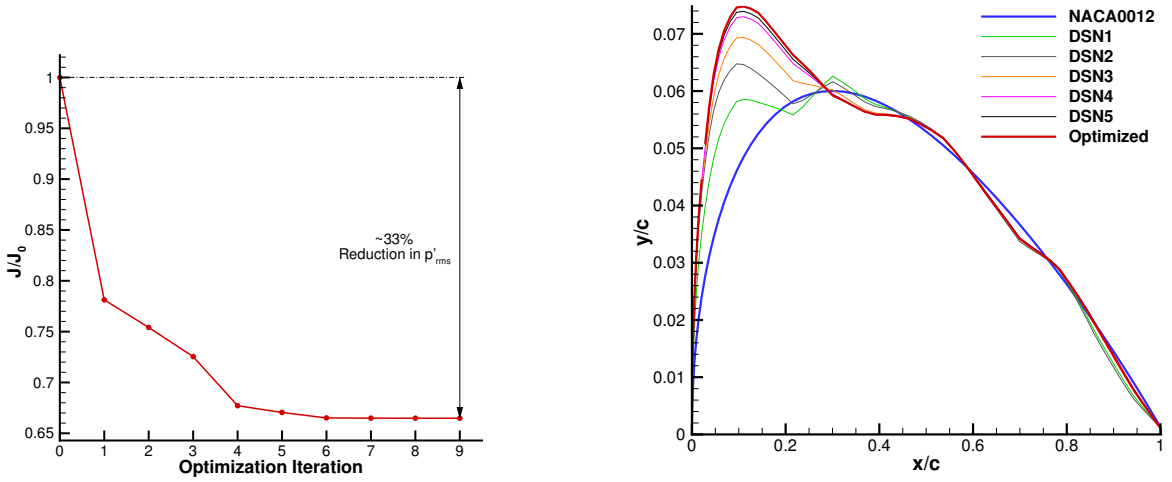


(a) Optimization Convergence History

(b) Evolution of Airfoil Shape

**Figure 6. (a): Convergence history of the optimization; (b): evolution of airfoil shapes during optimization (——: baseline NACA0012 profile; ——: optimized configuration). Note that y-axis is scaled to show the waviness of the new airfoil profile, particularly near the leading edge. Only the upper surface is plotted**

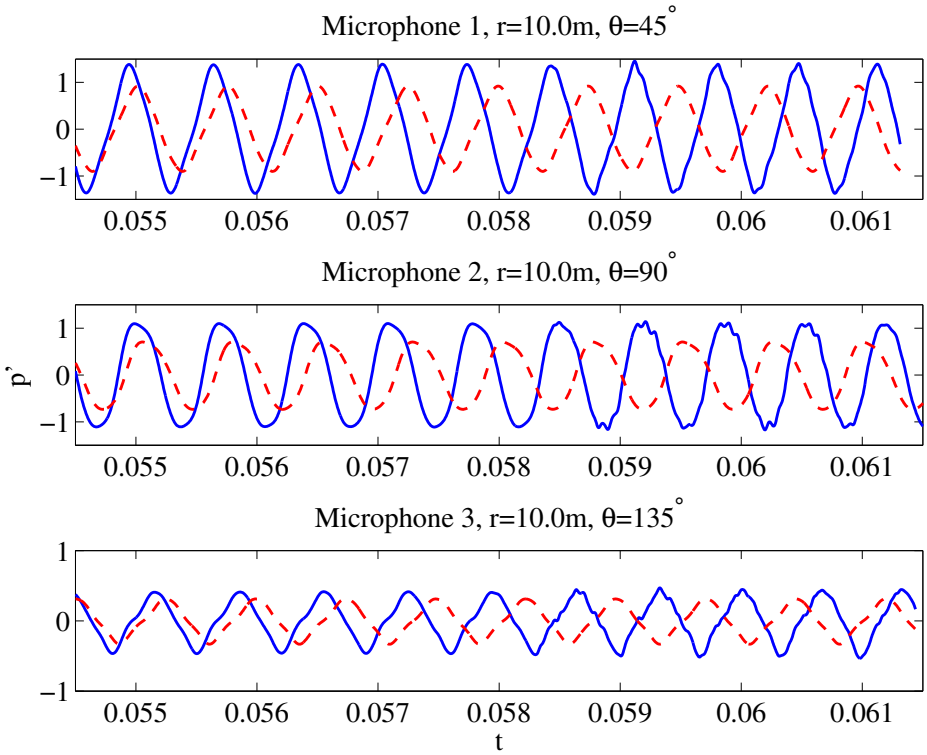


**Figure 7. Comparison of acoustic signals at three far-field microphone positions in the rod-airfoil case (——: baseline configuration with NACA0012 profile; – – –: optimized airfoil profile)**

broadband noise which cannot be accurately captured by URANS.

In the near future, we plan to first validate the two-step CFD-FWH noise prediction framework on more complex geometries such as that of a rudimentary landing gear (RLG) previously studied by Wang et al.[23] To that end, we will continue to leverage the parallel development on the detached-eddy simulation (DES) solver by other researchers in the SU2 community[24] and set up a coupled DES-FWH framework. The highly modular nature of the SU2 suite allows

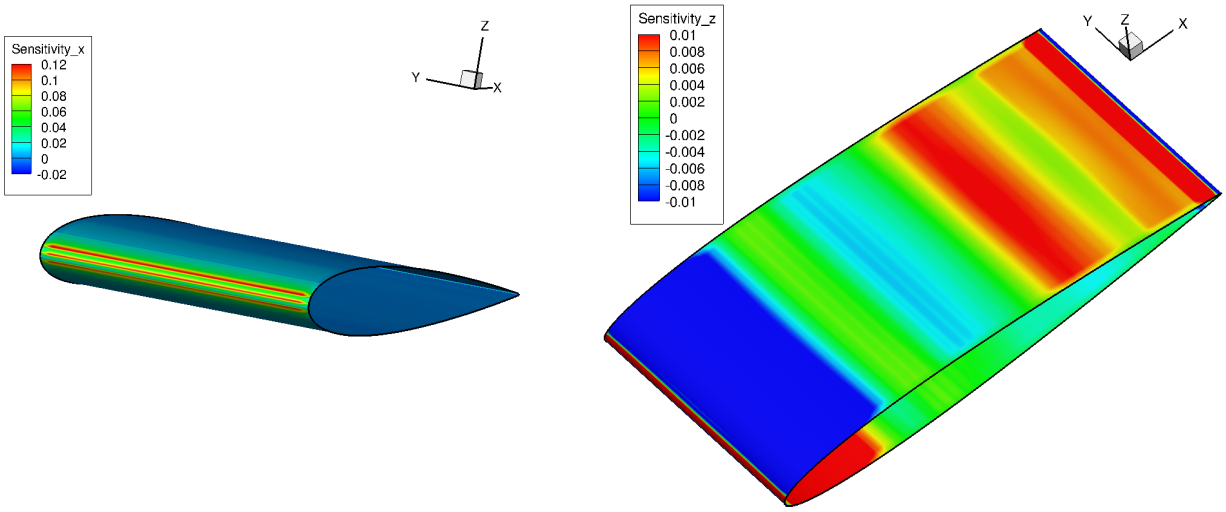


(a) Surface noise sensitivity in the streamwise direction

(b) Surface noise sensitivity in the normal direction

**Figure 8. Surface noise sensitivities in the streamwise (a) and normal (b) directions, computed for the baseline configuration**

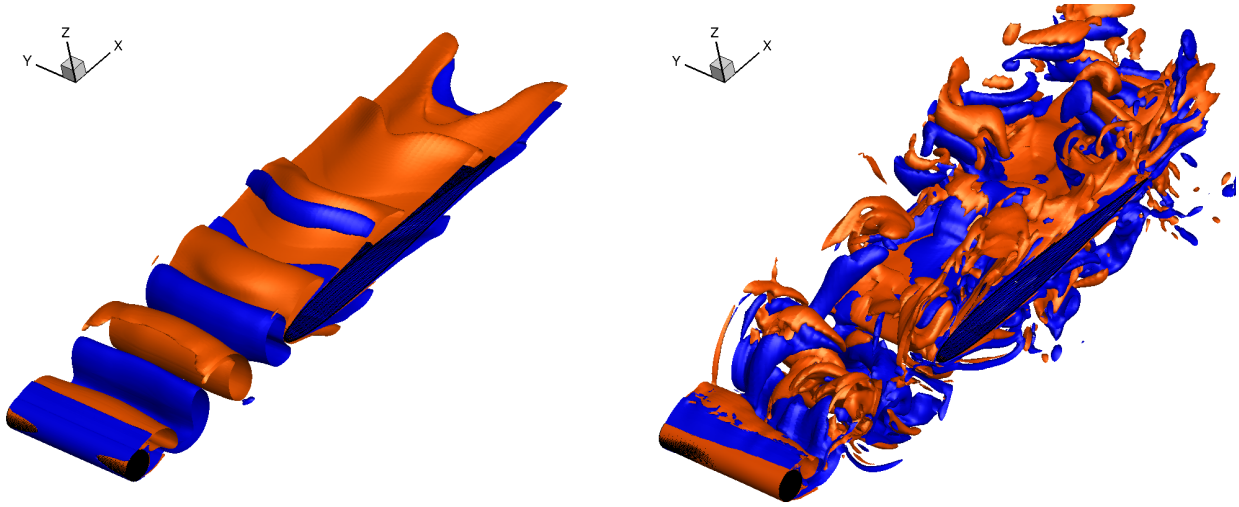


(a) URANS-SA

(b) DDES-SA

**Figure 9. Vorticity iso-surfaces ($\omega_z D/U_\infty = \pm 1$) of URANS-SA simulation (a) and DDES-SA simulation (b), both computed on the same mesh with 4.0 million elements**

the existing URANS solver to be easily replaced by the new DES solver. The FWH solver implemented in this work computes the far-field noise based on CFD data extracted from the permeable surface irrespective of the type of the underlying CFD solver.

With parallel development efforts from various SU2 contributors in other disciplines, we intend to extend this framework in the near future to address other inherently unsteady multi-physics design problems. For example, Sanchez et al.[26] have developed a fluid-structure interaction (FSI) solver in the SU2 framework. We envision that a synergy between our respective works in the near future will allow us to tackle a wide range of challenging problems in aerostructural design and vibroacoustics.

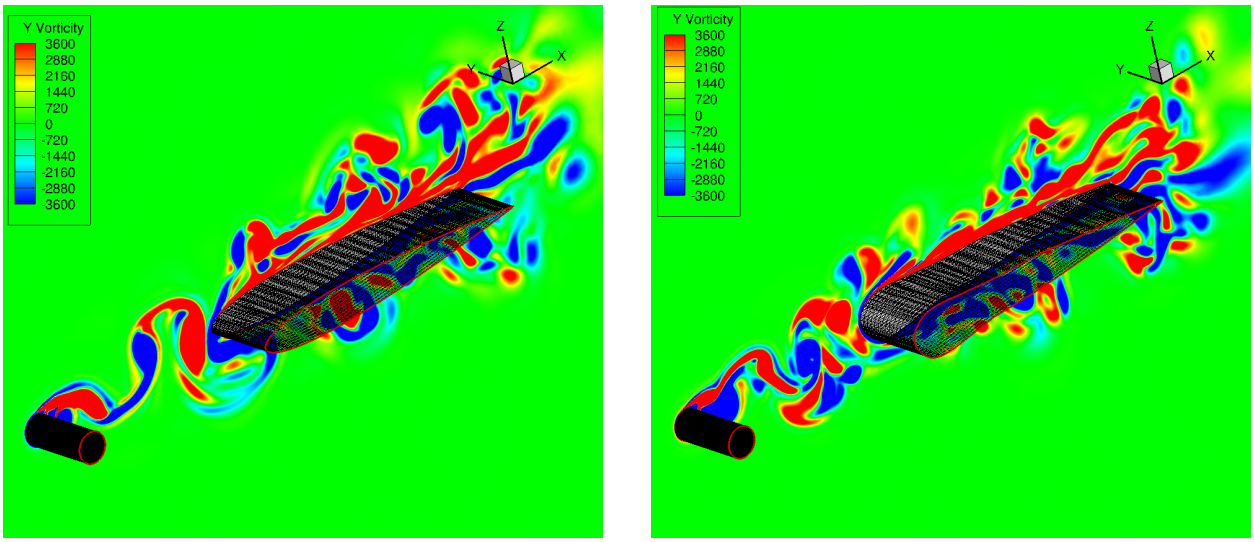


(a) Baseline (b) Optimized

**Figure 10. Spanwise vorticity field of the baseline (a) and the optimized (b) configurations, evaluated at mid-span**

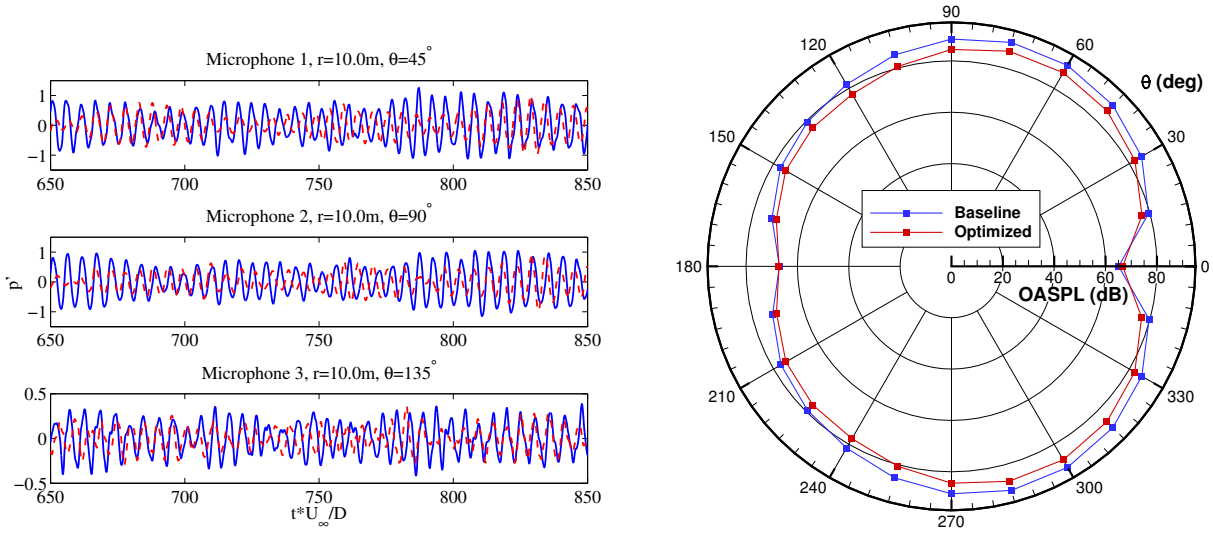


(a) Farfield Pressure Fluctuation (b) Overall Sound Pressure Level

**Figure 11. Comparison of the farfield pressure fluctuation at the three microphone positions (a). (——: baseline configuration with NACA0012 profile; – – – : optimized airfoil profile) and the overall sound pressure level (b)**

## VI. Acknowledgement

The first author would like to acknowledge the partial funding by the Natural Science and Engineering Research Council of Canada (NSERC). The authors would also like to gratefully acknowledge the RHRK high performance computing center for providing essential computational resources via the 'Elwetritsch' high performance cluster at the TU Kasierslautern.

## References

[1]Lockard D. P. and Lilley G. M. The Airframe Noise Reduction Challenge. *NASA Report*, (2004).

[2]Pironneau, O. On optimum design in fluid mechanics. *Journal of Fluid Mechanics* **64**, 97–110 (1974).

[3]Jameson, A. Aerodynamic design via control theory. *Journal of Scientific Computing* **3**, 233–260 (1988).

[4]Kenway, G. K. W. and Martins, J. R. R. A. Multipoint high-fidelity aerostructural optimization of a transport aircraft configuration. *Journal of Aircraft* **51** (1), 144–160 (2014).

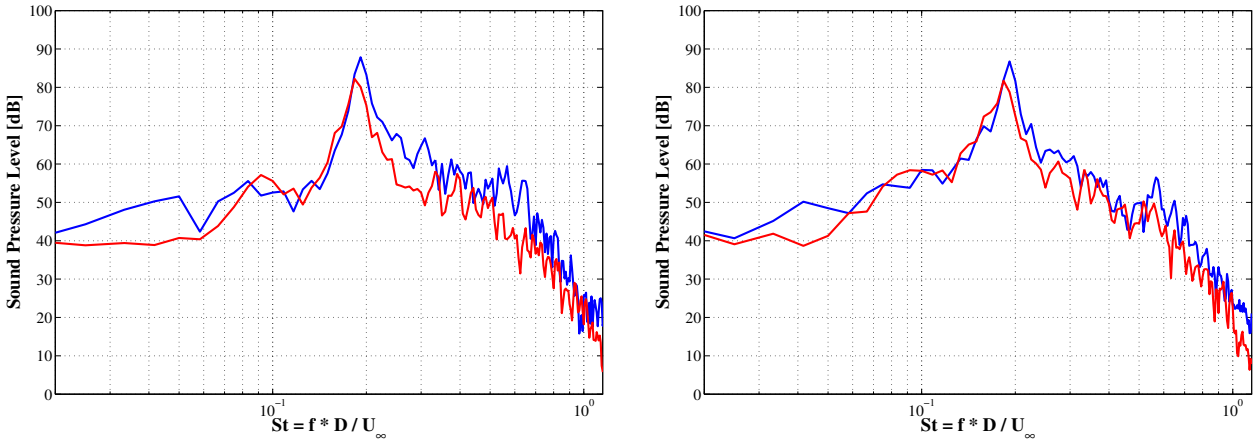


(a) $\theta = 45°$ (b) $\theta = 90°$

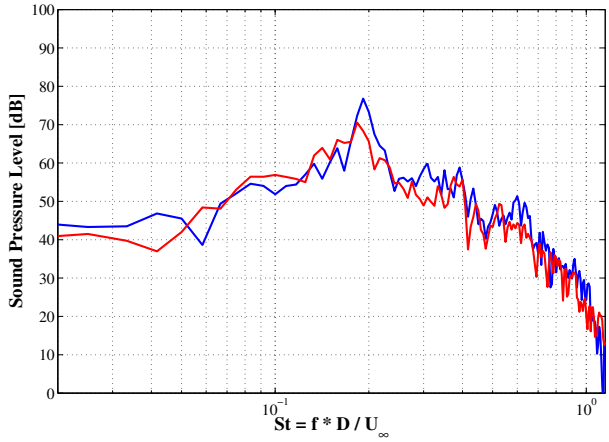


(c) $\theta = 135°$

**Figure 12. Comparison of sound pressure levels at three farfield microphone positions located at three angular positions $R = 100C$ from the leading edge mid-span point. (——: baseline configuration with NACA0012 profile; —— : optimized airfoil profile)**

[5]Lyu, Z. and Martins, J. Rockard. R. A. Aerodynamic design optimization studies of a blended-wing-body aicraft. *Journal of Aircraft* **51** (5), 1604–1617 (2014).

[6]Rumpfkeil, M. P. and Zingg, D. W. A hybrid algorithm for far-field noise minimization. *Computers and Fluids* **39**(9), 1516–1528 (2010).

[7]Mani, K. and Mavriplis, D. J. Unsteady discrete adjoint formulation for two-dimensional flow problems with deforming meshes. *AIAA Journal* **46**(6), 1351–1364 (2008).

[8]Nielsen, E. J. and Diskin, B. Discret adjoint-based design for unsteady turbulent flows on dynamic overset unstructured grids. *AIAA Paper*, 2012-0554 (2012).

[9]Economon, T. D., Palacios, F., and Alonso, J. J., A coupled-adjoint method for aerodynamic and aeroacoustic optimization. *AIAA Paper 2012-5598*, (2012).

[10]Economon, T. D., Palacios, F., and Alonso, J. J., An unsteady continuous adjoint approach for aerodynamic design on dynamic meshes. *AIAA Paper 2014-2300*, (2014).

[11]Hogan, R. Fast reverse-mode automatic differentiation using expression templates in C++. *Transactions on Mathematical Software* **40** (26), 1–16 (2014).

[12]Hovland, P., Mohammadi, B., and Bischof, C., Automatic differentiation and Navier-Stokes computations. *Computation Methods for Optimal Design and Control*, 265–284 (1998).

[13]Gauger, N. R., Walther, A., Moldenhauer, C., and Widhalm, M., Automatic differentiation of an entire design chain for aerodynamic shape optimization. *Notes on Numerical Fluid Mechanics and Multidisciplinary Design* **96**, 454–461 (2007).

[14]Nemili, A., Özkaya, E., Gauger, N., Kramer, F., Höll, T., and Thiele, F., Optimal design of active flow control for a complex high-lift Cconfiguration. *AIAA Paper 2014-2515*, (2014)

[15]Palacios, F., Economon, T. D., Aranake, A. C., Copeland, S. R., Lonkar, A. K., Lukaczyk, T. W., Manosalvas, D. E., Naik, K. R., Padron, A. S., Tracey, B., Variyar, A., and Alonso, J. J., Stanford University Unstructured (SU2): Open-source analysis and design technology for turbulent flows. *AIAA Paper 2014-0243*, (2014)

[16]Colonius, T. and Lele, S. K. Computational Aeroacoustics: Progress on Nonlienar Problems of Sound Generation. *Progress in Aerospace Sciences* **40**, 345–416 (2004).

[17]Lockard, D. P., An Efficient, Two-Dimensional Implementation of the Ffowcs Williams and Hawkings Equation. *Journal of Sound and Vibration* **229**(4), 897–911 (2000).

[18]Di Francescantonio, P., A New Boundary Integral Formulation for the Prediction of Sound Radiation. *Journal of Sound and Vibration* **202**(4), 491–509 (1997).

[19]Lyrintzis, A. S., Surface integral methods in computational aeroacoustics – From the (CFD) near-field to the (Acoustic) far-field. *International Journal of Aeroacoustics* **2**(2), 95–128 (2003).

[20]Griewank, A., and Walther, A., Evaluating Derivatives: Principles and Techniques of Algorithmic Differentiation. *Other Titles in Applied Mathematics*, SIAM, 9780898716597., (2008).

[21]Nemili, A., Özkaya, E., Gauger, N. Carnarius, A., Thiele, F., Optimal Control of Unsteady Flows Using Discrete Adjoints. *AIAA Paper 2011-3720*, (2011)

[22]Zhou, B. Y., Albring, T. A., Gauger, N. R., Ilario da Silva, C. R., Economon, T. D., Alonso, J. J., An Efficient Unsteady Aerodynamic and Aeroacoustic Framework Using Discrete Adjoint. *AIAA Paper 2016-3369*, (2016)

[23]Wang, L., Mockett C., Knacke, T., Thiele, F., Detached-Eddy Simulation of Landing-Gear Noise *AIAA Paper 2013-2069*, (2013)

[24]Molina, E. S., Spode, C., da Silva, R. G., Manosalvas-Kjono, D. E., Nimmagadda, S., Economon, T. D., and Alonso J. J., Hybrid RANS/LES Calculations in SU2, *The 18th AIAA/ISSMO Multidisciplinary Analysis and Optimization Conference, Submitted*, (2016)

[25]Lockard, D. P. and Casper, J. H., Permeable Surface Correction for Ffowcs Williams and Hawkings Integrals *AIAA Paper 2005-2995*, (2005)

[26]Sanchez R., Palacios R., Economon T. D., Kline H., Alonso J. J., Palacios F., Towards a Fluid-Structure Interaction Solver for Problems with Large Deformations within the Open-Source SU2 Suite *AIAA Paper 2016-0205*, (2016)

[27]Dowling, A. P. and Ffowcs Williams, J. E., Sound and Sources of Sound, *Ellis Horwood Publishers*, (1983)